Coarse-grain modelling of DMPC and DOPC lipid bilayers

Coarse-grain modelling of DMPC and DOPC lipid bilayers

Mario Orsi, Julien Michel[1] and Jonathan W Essex

School of Chemistry, University of Southampton, Southampton SO17 1BJ, UK

E-mail: j.w.essex@soton.ac.uk

Abstract
Our recently developed coarse-grain model for dimyristoylphosphatidylcholine (DMPC) has been improved and extended to dioleylphosphatidylcholine (DOPC), a more typical constituent of real biological membranes. Single-component DMPC and DOPC bilayers have been simulated using microsecond-long molecular dynamics. We investigated properties that are difficult or impossible to access experimentally, such as the pressure distribution, the spontaneous curvature and the diffusion pattern of individual lipid molecules. Moreover, we studied the dipole potential, a basic physical feature of paramount biological importance that cannot be currently modelled by other coarse-grain approaches. In fact, a complete representation of the system electrostatics and a realistic description of the water component make our method unique amongst the existing coarse-grain membrane models. The spontaneous permeation of water, a phenomenon out of reach of standard atomistic models, was also observed and quantified; this was possible thanks to the efficiency of our model, which is about two orders of magnitude less computationally expensive than atomic-level counterparts. Results are generally in good agreement with the literature data. Further model extensions and future applications are proposed.

(Some figures in this article are in colour only in the electronic version)

1. Introduction

Coarse-grain (CG) simulation models of biomolecular systems, and particularly lipid membranes, have recently become remarkably popular [1–3]. CG techniques are typically orders of magnitude less demanding of computational resources than standard atomic-level models, thus allowing the study of a much larger range of properties and phenomena. To achieve high efficiency, CG models must sacrifice detail; typically, clusters of several atoms are reduced to individual macroparticles. Different levels of granularities are possible; to set a relevant background for the work presented in this paper, in this initial section we discuss some aspects of those CG models where single lipid molecules, which in reality comprise ≈100 atoms, are coarse-grained to collections of ≈10 sites [4–8]. In particular, we will mainly focus on how these models approximate the solvent environment (water) and the electrostatic properties (charges). These two aspects

are considered in turn in the following paragraphs; potential problems are highlighted regarding specific properties and phenomena. This discussion is clearly not intended to be an exhaustive review of the available models, but only an account of some issues that we believe should be considered carefully when addressing particular problems by CG methods. In general, each CG model is designed to achieve specific targets, will be especially suitable to address certain types of problems, and will also inherently be characterized by particular limitations (as is true for any model based on empirical force fields). It is therefore important to be aware of the differences between the various available methods so as to choose the most appropriate one for a particular problem of interest.

Water, the universal biological solvent, is traditionally a challenging substance to model, due to its peculiar characteristics (such as its large dipole relative to molecular size and its hydrogen bonding properties). Additional difficulties should be expected when modelling water by simplified methods. CG water is often described by apolar

---

[1] Present address: Department of Chemistry, Yale University, New Haven, CT 06520-8107, USA.

1

solvent macroparticles, each accounting for a group of three or four water molecules [4, 5, 7]. Real water molecules are highly polarized, and this feature is responsible for fundamental processes such as the screening of charged particles (e.g., lipid headgroups and ions) or the generation of electric fields (e.g., at the interface with the membrane); these characteristics are therefore lacking from most CG models. An extreme example of the potential issues deriving from an oversimplified solvent description is the recent finding that the CG water in the popular MARTINI model [7] is solid at physiological temperatures [9].

Electrostatic features also tend to be heavily approximated in CG models. Electrostatic interactions represent a major component of the intermolecular interactions in most (bio)molecular systems, and hence their approximation should be considered carefully. As already noted, CG water models do not normally contain charges [4, 5, 7]. In some cases, there is no explicit description of any charged component of the system [5, 6]. Some CG models only include explicit charges in the lipid headgroup [4, 7], while they lack charges in the glycerol–ester region. While it could be argued that most properties depending on electrostatic interactions can be captured sufficiently well, in a CG context, even without an explicit charge representation (for instance through ad hoc tuning of Lennard-Jones potentials), an important inevitable issue is that incomplete electrostatic descriptions [4–7] would result in unphysical representations of the dipole potential, a fundamental membrane property which characterizes the electrostatic potential difference between the water phase and the bilayer hydrocarbon core [10]. The total dipole potential comprises contributions from the various charged components. In PC lipids, the headgroup dipoles point their positive end towards water and their negative end towards the bilayer core, thus leading to a negative contribution to the total dipole potential. The alignment of water and ester–glycerol dipoles overcompensates the headgroup effect, eventually leading to the generation of a net positive value for the total dipole potential, as established experimentally [11–13]. Those CG models [4, 7] that only comprise headgroup electrostatics would therefore wrongly yield a negative dipole potential. This problem has been surprisingly overlooked so far, given the importance of the dipole potential for numerous fundamental biological processes [10, 14–25].

To address the issues discussed, we have recently introduced a CG model containing a number of important novel features [8]. In particular, we have adopted a single-site water model [26] which contains an explicit representation of the water dipole; this model represents accurately all fundamental physical properties of liquid water [27–29]. Moreover, we explicitly include the relevant lipid electrostatics by charges in the headgroup and dipoles in the glycerol–ester region. It is therefore possible to adequately describe the membrane dipole potential. In fact, the electrostatic distribution of the original model somewhat overestimated the experimental dipole potential; this issue has been successfully tackled (as reported in section 3), and the dipole potential of our model is now in quantitative agreement with experiment (section 5.4).

In general, our original model proved capable of reproducing the major physical features of dimyristoylphosphatidylcholine (DMPC) lipid bilayers [8]. We chose DMPC as a starting point for a number of reasons. First, DMPC belongs to the family of glycerophospholipids, representing the main lipid components of biological membranes [30]. Moreover, DMPC lipid bilayers have been well characterized by experimental methods; many physical parameters are therefore available to validate the computational model. Also, DMPC is a lipid with a simple structure, because the hydrocarbon tails only comprise single bonds. Hence DMPC is a reasonable starting point for developing cell membrane models. However, real membrane lipids are typically longer; in fact, while DMPC tails comprise fourteen carbons, the most common fatty acids chain lengths fall between fourteen and twenty-two [31]. Moreover, unlike DMPC, the majority of real lipids contain double bonds (unsaturations) along their tails. We therefore decided to extend the CG model to dioleylphosphatidylcholine (DOPC), one of the most typical cell membrane lipids; in fact, each tail is eighteen carbon long and contains one double-bond in its centre.

This paper focuses on the refinement of our original CG model for DMPC [8] and its extension to DOPC. The new force field is parametrized concurrently for the two lipid species, hence facilitating transferability. In section 2 we describe the main features of the lipid models, including particularly the extra parameters introduced to represent the DOPC double bonds. The following section 3 reports on the parametrization procedure. The simulation protocol is detailed in section 4. Results are subsequently presented and discussed (section 5); comparisons are made with experimental and simulation data from the literature. The main conclusions and potential future extensions are summarized in section 6.

2. Lipid models

2.1. DMPC

In our CG approach [8], the DMPC lipid molecule is represented by ten sites; given that a real DMPC molecule comprises 118 atoms, the coarse-graining process corresponds to a reduction of the number of particles by a factor of ≈ 10. Specifically, the lipid headgroup is coarse-grained into two spherical units, describing the choline and phosphate moieties; these particles interact through the (standard) Lennard-Jones potential. Headgroup electrostatics are represented explicitly by a positive point-charge embedded in the choline site and a negative one in the phosphate site. The glycerol and hydrocarbon regions of the lipid are modelled as soft uniaxial ellipsoids through the Gay–Berne potential [32]. The Gay–Berne model, which can be considered an extension of the spherically-symmetric Lennard-Jones potential, is typically used to represent rod-like and disk-like particles. In particular, the glycerol–ester region is described by two Gay–Berne ellipsoidal units, each embedded with a point-dipole to capture the dipolar charge distribution in this region. Hydrocarbon tails are modelled by chains of three neutral Gay–Berne ellipsoids [33]; each ellipsoid represents a segment of four

138 atoms $\Longrightarrow$ 12 coarse-grain sites
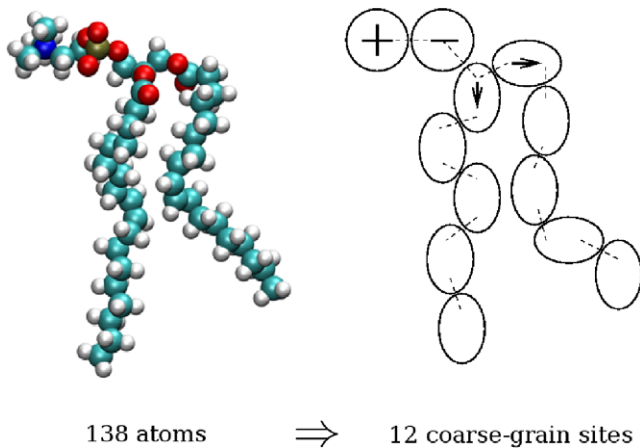
Figure 1. DOPC coarse-graining. The left molecule is an all-atom representation of a DOPC lipid. The corresponding CG model is depicted on the right. CG electrostatics are highlighted; they comprise positive ('+' sign) and negative ('−' sign) point-charges in the headgroups, and point-dipoles (arrows) in the glycerol–ester sites. Harmonic springs, representing CG covalent bonding, are also shown (dashed segments).

consecutive CH_2 groups. Intra-lipid bonds are modelled by the Hooke (harmonic) potential, as is standard practice. No angle or torsional potentials are present. More details and a sketch illustrating the DMPC coarse-graining can be found in our original publication [8].

2.2. DOPC

The DOPC molecule is longer than DMPC (18 carbons versus 14) and comprises a double-bond, or unsaturation, in the middle of each of the two tails (whereas DMPC contains exclusively single bonds). Our CG model for DOPC has been easily derived from the DMPC model by adding a Gay–Berne particle at the bottom of each tail; since each of these particles corresponds to four CH_2 groups, the added sites consistently describe the 4-carbon difference in length between DMPC and DOPC. An illustration of the coarse-graining process is reported in figure 1. The unsaturations in DOPC are modelled through an angular potential that restrains the mutual orientations of the two central Gay–Berne sites in each tail. In particular, if θ_{ij} is the angle between the two vectors along the main axis of each of the two Gay–Berne sites i and j, the potential u_{ij} can be written as:

$$u_{ij} = \frac{k_{\theta_{ij}}}{2}(\cos\theta_{ij} - \cos\theta_0)^2 \qquad (1)$$

with $k_{\theta_{ij}}$ the rigidity constant and θ_0 the reference angle. The corresponding forces and torques, necessary to the molecular dynamics algorithm, are derived in appendix A.

3. Parametrization

The force field parameters have been optimized to reproduce the experimental measurements of some of the most important physical properties of lipid bilayers, that is, lipid area and

volume, dipole potential and spontaneous curvature. The lipid area and volume represent the most basic membrane structural features, and were also used to parametrize the original model [8]. The membrane dipole potential [10] is involved in a large number of biological processes, such as membrane fusion [14], permeation [15], the regulation of membrane proteins (Na^+-K^+-ATPase [16], gramicidin [17], phospholipase A_2 [18]), insertion and folding of amphiphilic peptides [19], the kinetics of DNA–lipid complexes [20], the kinetics of redox reactions at membrane surfaces [21], human skin permeability [22], general anaesthesia [23], the binding capacity of drugs [24], and the modulation of molecule–membrane interactions in lipid rafts with possible effects on cells signalling [25]. The (monolayer) spontaneous curvature is at the basis of phase transitions and fusion [34], and is believed to be involved in controlling the function of many membrane proteins [35], with effects on phenomena such as anaesthesia [23], lipid biosynthesis [36] and vision [37].

The force field optimization involved the incremental refinement of selected parameters by trial simulations. The starting point was the parameter set originally developed for our DMPC model [8]. That force field yielded a dipole potential too large by a factor of ≈ 3 compared to the experimental data [11, 12]. To match the experimental results, we introduced two modifications to the original model [8]. First, the magnitude of the ester–glycerol dipoles was reduced from 3D to 1D; this reduces their contribution to the overall potential, in turn lowering the total value. Second, the Lennard-Jones interaction energy between choline and glycerol sites was reduced by 20% through a scaling of the cross term:

$$\epsilon_{CG} = \sqrt{\epsilon_{CC}\,\epsilon_{GG}}/1.2 \qquad (2)$$

where the ϵ constants represent the Lennard-Jones energy well depths, and subscripts C and G stand for choline and glycerol, respectively. This modification, which induces an effective repulsion between choline and glycerol groups, not only contributes to lower the overall value of the dipole potential, but also induces the headgroup dipole to point, on average, slightly towards the water phase outside the bilayer, as observed experimentally [38]; we have therefore corrected another inaccuracy of the original model, which yielded instead a headgroup vector slightly pointing towards the bilayer centre [8].

To reproduce the monolayer spontaneous curvature, we could simply fine-tune the Lennard-Jones and Gay–Berne parameters. The spontaneous curvature is a quantity characterizing the monolayer tendency to bend away from its flat configuration. This tendency can be related to the lipid shape; for example, large headgroups and short tails normally increase the tendency to curl away from the water phase and form micellar structures, whereas small headgroups and long tails typically increase the tendency to curl towards the water phase and form inverted lipid phases. The experimental data for the spontaneous curvature could therefore be targeted by tuning the size of the lipid particles. The rigorous definition of spontaneous curvature will be given in section 5.3.

Finally, the extra parameters introduced to model the DOPC double-bond (defined previously in equation (1)) have

been optimized by targeting the DOPC lipid area. All force field parameters are collected in table B.1 of appendix B. For a description of the terms not discussed here we refer to the original article [8].

4. Protocol

Two hydrated bilayer systems, one comprising DMPC lipids and the other comprising DOPC lipids, were prepared. The DMPC system included 128 lipids and 5000 water molecules (hydration level of 50 wt%), and the DOPC system included 128 lipids and 5760 water molecules (hydration level of 52 wt%). The water content was set to ensure full hydration of the bilayer, as in the experimental systems considered for comparison. Both bilayers comprised an equal number of lipids (64) in each monolayer. Molecular dynamics simulations were conducted using our software BRAHMS [39], which implements the advanced rigid-body integrator of Dullweber *et al* [40]; the integration time step was 20 fs. Pressure and temperature were maintained at 1 atm and 30 °C using the weak-coupling scheme [41]. Lipid and water temperatures were coupled separately with time constants $\tau_T = 0.1$ ps; for rigid-body sites, translational and rotational degrees of freedom were coupled independently. The pressure was controlled by semi-isotropic volume scaling, meaning that the normal and tangential components of the pressure tensor were regulated separately. In particular, the pressure along the z-axis, that is, along the direction normal to the interface, was controlled by rescaling the z-dimension of the simulation region, whereas the tangential pressure was controlled by rescaling the xy area, with the constraint that the interface remained a square. The pressure-coupling time constant was $\tau_P = 0.2$ ps, and the isothermal compressibility was $\beta = 4.6 \times 10^{-5}$ atm^{-1}. The cutoff radius for both Lennard-Jones and electrostatic water–water interactions was 0.9 nm, as prescribed for the SSD parametrization adopted [28]. All other non-bonded cutoff radii were set to 1.2 nm. Electrostatic interactions were treated using cutoff schemes. In particular, all charge–charge and charge–dipole interactions were implemented using the shifted-force cutoff method [42]. We employed the SSD parameters optimized to evaluate dipole–dipole interactions with a cubic switching cutoff scheme [28]; for consistency, all dipole–dipole interactions were treated in this manner. Masses and moments of inertia are set as in the original model [8]. In particular, the masses of the CG lipid sites reproduce the sum of the atomic masses of the corresponding clusters of atoms; it follows that the total mass of each CG lipid molecules corresponds to the real mass. For the ellipsoidal rigid-body units, the principal moments of inertia are assigned assuming uniform density. As in our original protocol [8], the mass and principal moments of inertia of water sites are increased to optimize the stability of molecular dynamics integration. In particular, the mass of every CG water site is set to 50 amu. Thermodynamic properties are not affected by such an alteration of the inertial features of water. However, dynamics are intuitively predicted to be somewhat slower. We showed previously [8] that the diffusion coefficient of our

'heavy' water is $\approx$20% smaller than the experimental value (and $\approx$30% smaller than the value calculated for SSD with the original correct mass [28]). A complete listing of the inertial parameters is included in table B.1 of appendix B. After initial equilibration runs lasting 100 ns, over which time the bilayers' area and volume stabilized around their equilibrium values, we simulated both DMPC and DOPC systems for 1.2 μs each. The simulations were run in serial on Intel 2.8 GHz processors; sampling speed was $\approx$20 ns day^{-1}.

5. Results and discussion

In this section, we report and discuss the membrane physical properties calculated with our CG models for DMPC and DOPC bilayers. The reported average values and standard errors were computed from two subaverages taken over the two 0.6 μs consecutive blocks of the 1.2 μs trajectories, unless otherwise stated. The analysis of a number of properties was carried out following a general process that involves 'slicing' the system along planes perpendicular to the z axis (interface normal). In particular, we defined 70 slices of thickness $\Delta z \approx 0.1$ nm, the actual value of Δz being evaluated at every step to account for the fluctuations of the z-dimension of the simulation region. Several bilayer properties are homogeneous inside a particular slice, due to the intrinsic axial symmetry of the system. Therefore single curves, *profiles* evaluated as a function of z, provide full characterization. The slicing procedure was employed to calculate the following profiles: electron density, lateral pressure and electrostatic potential. We report the average profiles obtained from calculation at every molecular dynamics integration step over the whole 1.2 μs measurement time. No extra processing was done, that is, no filters were applied to smooth the curves, and we did not average over the two monolayers. It will be seen that the profiles are nonetheless smooth (almost noise-free) and symmetrical. This is indicative of a well-equilibrated system and adequate sampling. Simulation results will be primarily compared to experimental measurements; if not otherwise stated, all data reported for comparison refer to systems and conditions consistent with our simulations, that is, fully-hydrated liquid-phase DMPC and DOPC bilayers at 30 °C. For easy reference, all the quantitative results obtained are collected in tables C.1 and C.2 in appendix C, together with corresponding experimental data.

5.1. Structure

5.1.1. Lipid area and volume. For DMPC, the calculated lipid volume is $V_L = 1.0917 \pm 0.0001$ nm^3, consistent with the experimental value of 1.101 nm^3 [43]; the lipid area is $A_L = 61.59 \pm 0.04$ Å^2, slightly larger than the experimental values of 60.6 Å^2 [43] and 59.7 Å^2 [44]. Regarding DOPC, we obtained $V_L = 1.3057 \pm 0.0001$ nm^3, in agreement with the experimental value of 1.303 nm^3 [45, 46], and $A_L = 69.54 \pm 0.15$ Å^2, consistent with the experimental range of measurements of 67.4–72.5 Å^2 [45–47, 50, 51].

5.1.2. Compressibility moduli. From the fluctuation of the volume and area it is possible to estimate the compressibility moduli. In particular, the volume compressibility modulus K_V can be computed as $K_V = k_B T V / \sigma^2(V)$, V and $\sigma^2(V)$ being respectively the mean and mean squared fluctuation of the volume of the simulation region. The area compressibility K_A can be computed from simulation as $K_A = k_B T A / \sigma^2(A)$, A and $\sigma^2(A)$ being respectively the mean and mean squared fluctuation of the interfacial area. We calculated for DMPC $K_V = 12.43 \pm 0.02$ kbar, consistent with the experimental range 10–30 kbar reported as typical for fluid-phase phospholipid bilayers [52], and $K_A = 166 \pm 22$ dyn cm^{-1}, a value somewhat lower than the experimental measurement of 234 dyn cm^{-1} [53]. For the original model [8], we obtained a value of 297 dyn cm^{-1}, hence larger than that calculated for the current model. This discrepancy is likely to depend, in substantial part, on a sensitivity of K_A to the various force field parameters that have been updated; unfortunately, there is no clear way to quantify individual effects of the different parameters. Another factor that may have contributed to the observed discrepancy is the difference in simulation times. The previous calculation [8] was performed over two 100 ns blocks of a 200 ns trajectory, whereas for this work we used two 600 ns blocks of a 1.2 μs trajectory. Area fluctuations are expected to be sampled more thoroughly the longer the trajectory. Hence, in the original model, $\sigma^2(A)$ might have been underestimated; since this quantity is the denominator of the expression used to calculate K_A, its undersampling could have lead to an overestimation of K_A. We investigated this effect by recalculating the current model's K_A from twelve 100 ns blocks of the 1.2 μs trajectory; the obtained value of 184 ± 7 dyn cm^{-1} is indeed slightly larger than the value of 166 dyn cm^{-1} calculated from the 600 ns blocks. For DOPC, we calculated $K_V = 12.84 \pm 0.04$ kbar, again consistent with the typical experimental range of 10–30 kbar [52], and $K_A = 366 \pm 9$ dyn cm^{-1}, somewhat higher than the experimental measurements of 188 [50] and of 265 dyn cm^{-1} [53].

5.1.3. Headgroup dipole. The headgroup dipole moment can be defined as $\boldsymbol{\mu}_{HG} = q\mathbf{d}$, with $\mathbf{d}$ the instantaneous vector connecting the phosphate to the choline mass centre and q the (equal) absolute magnitude of each headgroup charge. Owing to the lack of experimental data for the headgroup dipole of DMPC and DOPC, we compare the results of our model with measurements on dipalmitoylphosphatidylcholine (DPPC) bilayers [38, 54]. DPPC is structurally rather similar to DMPC and DOPC; also, the experiments considered [38, 54] were carried out on fully-hydrated bilayers in the fluid-phase, under the same conditions as our simulation. Therefore it is reasonable to compare our results with these experimental data. We calculate a dipole magnitude of ≈17.8 D for both DMPC and DOPC, in good agreement with the experimental estimate of 18.7 D [54]. As for the headgroup inclination from the membrane normal, we obtained values of ≈89° for both our lipids; this is broadly consistent with the experimental estimation of a preferred conformation at ≈72° from the membrane normal [38]. In particular, these data indicate that the headgroup dipole lies approximately flat on the membrane plane, in fact very slightly pointing towards the water phase.
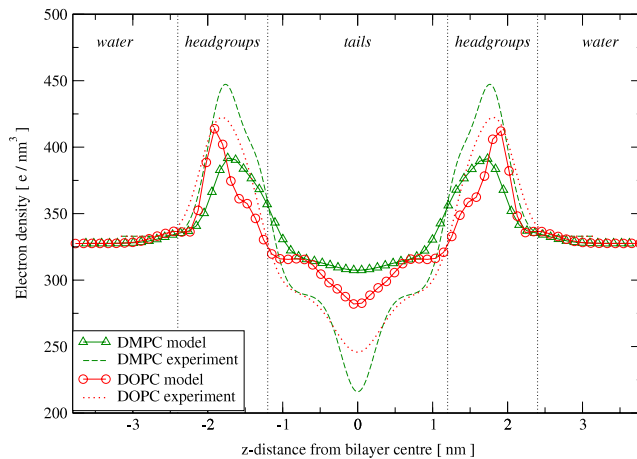
Figure 2. Electron density profiles. The distributions calculated with our model are superimposed on corresponding experimental profiles [43, 47]. To facilitate interpretation, different regions across the system are marked in italics, namely, the bulk *water* region, the lipid *headgroups* region and the lipid hydrocarbon *tails* core. Approximate boundaries between these regions are defined by the vertical dotted lines.

5.1.4. Electron density. To estimate the electron density profile along the bilayer normal, the lipid electrons were distributed to each CG site to match as closely as possible the underlying real electron locations, taking care that the total number of electrons per lipid in the models equals the real value (374 for DMPC and 434 for DOPC). In particular, we placed the 50 electrons of the choline cluster and the 55 electrons of the phosphate clusters at the mass centre of the corresponding CG units. As for the ellipsoidal particles that constitute the rest of the lipid in our representation, we distributed electrons over four positions evenly spaced along the principal axis of each ellipsoid. In particular, assuming that the ellipsoids' dimension along the principal axis measures $\kappa\sigma_{TT}$, with κ and σ_{TT} defined in table B.1 of appendix B, the four positions are spaced $\kappa\sigma_{TT}/4$ apart. The 38 electrons of the CG glycerol–ester site at the top of the $S_n 1$ tail can be grouped into four clusters, corresponding to the glycerol CH$_2$ group (8 electrons), the oxygen (8 electrons), the CO group (14 electrons) and the top CH$_2$ group of the aliphatic tail (8 electrons). These four clusters of electrons were mapped to the four locations defined above along the corresponding CG glycerol-ester ellipsoidal site. Similarly, the second CG glycerol–ester site, representing the top of the $S_n 2$ tail, was assigned 37 electrons, distributed over the four predefined locations which in this case are mapped to the glycerol CH group (7 electrons), the oxygen (8 electrons), the CO group (14 electrons) and the top CH$_2$ group of the aliphatic tail (8 electrons). For the hydrocarbon tail sites, the distributions are straightforward, as each CG site generally represents a segment of four CH$_2$ groups (each bearing 8 electrons). Exceptions were adequately taken into account for the DOPC unsaturations (where CH groups were assigned 7 electrons each) and for the last positions at the end of each tail (where CH$_3$ groups were assigned 9 electrons each). The calculated electron density profiles are reported in figure 2, along with

corresponding experimental data [43, 47]. The results from our simulations are qualitatively consistent with the experimental measurements. In particular, the electron density maxima corresponding to the headgroup regions and the minimum at the bilayer centre are qualitatively reproduced. Also, the head-to-head distances d_{HH}, which correspond to the distance between the maxima and define the bilayer thicknesses, are broadly consistent with the experimental results; we obtained 3.467 ± 0.003 nm for DMPC, in good agreement with the measurement of 3.53 nm [43], and 3.820 ± 0.008 nm for DOPC, slightly higher than the experimental values of 3.53 [50], 3.67 [45, 46] and 3.71 nm [47]. However, there are clear discrepancies between the experimental curves and our data in terms of electron density magnitudes; in particular, our current model underestimates the maxima and minima, especially for DMPC. In fact, in this respect our original model was performing better [8]. This is not surprising, since we have reparametrized the force field without attempting to fit the experimental density profile. We believe that the deterioration of this property is a comparatively minor disadvantage, far outweighed by the overall force field improvements, in terms of transferability to DOPC, and in terms of better results obtained for the headgroup structure and especially for the electrostatic potential (see section 5.4). Single-site density profiles have also been analysed; results are similar to those obtained for the original model [8]. In particular, the water density profiles highlight substantial headgroup hydration, as well as significant penetration of water molecules up to a distance of ≈ 1 nm from the bilayer centre (corresponding to the glycerol and upper tail regions); our data are consistent with AL results [48, 49].

5.1.5. Bending rigidity moduli.

The bilayer bending modulus κ^{b} can be related to the area compressibility modulus K_{A} via $\kappa^{b} = K_{A} d_{t}^{2}/24$, the 'effective' bilayer thickness d_{t} being $d_{t} = d_{HH} - 1$ nm, with d_{HH} the peak-to-peak distance in the electron density profile [53]. For DMPC, using K_{A} and d_{HH} from our previous results, we obtained $\kappa^{b} = 10.4 \pm 0.3 \, k_{B}T$. Experiments measured similar values of $13.5 \, k_{B}T$ from pipette aspiration [53] and $16.7 \, k_{B}T$ from x-ray data [55]; however, somewhat larger values of $31.4 \, k_{B}T$ and $32.1 \, k_{B}T$ were obtained from thermally excited shape fluctuation [56] and all-optical measurement [57], respectively. For DOPC, we calculated $\kappa^{b} = 30.0 \pm 1.0 \, k_{B}T$. Reported experimental data are in this case slightly smaller; values of $18.8 \, k_{B}T$ [46] and $19.8 \, k_{B}T$ [47] were obtained from x-ray scattering, whereas a value of $21.0 \, k_{B}T$ was obtained from pipette aspiration [53].

5.2. Pressure distribution

The internal pressure distribution, also known as the 'lateral pressure profile', can be defined as the difference between the lateral and normal components of the pressure tensor as a function of the coordinate z along the direction normal to the interface plane. In particular, considering the diagonal elements of the pressure tensor $P_{xx}(z)$, $P_{yy}(z)$ and $P_{zz}(z)$, the 'lateral' pressure is calculated as $P_{L}(z) = [P_{xx}(z) + P_{yy}(z)]/2$, and the 'normal' pressure is simply $P_{N}(z) = P_{zz}(z)$.
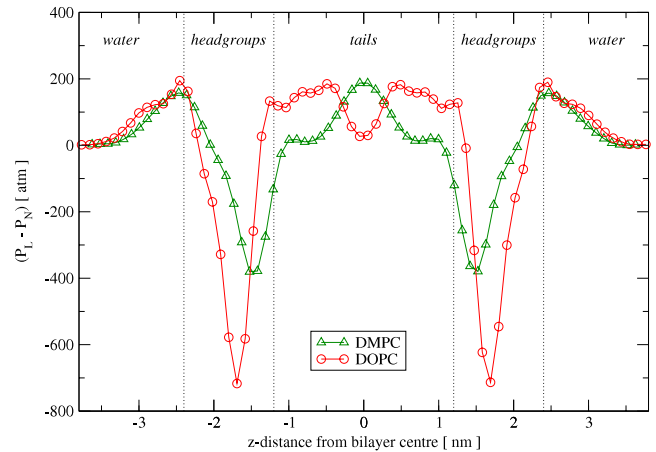
Figure 3. Lateral pressure profiles. To facilitate interpretation, different regions across the system are marked in italics, namely, the bulk *water* region, the lipid *headgroups* region and the lipid hydrocarbon *tails* core. Approximate boundaries between these regions are defined by the vertical dotted lines.

Conventionally, the 'lateral pressure profile' is defined as the difference $P_{L}(z) - P_{N}(z)$. The lateral pressure profiles for our bilayer models, evaluated using the Harasima contour [58], are reported in figure 3. For both the DMPC and DOPC pressure distributions, the magnitude in the water phases (at the left and right extremes of the curves) is zero, as expected for bulk water at mechanical equilibrium (the diagonal components of the pressure tensor being equal). The pressure then rises until a maximum of ≈ 200 atm corresponding to the interface between the water and lipid headgroup regions. This positive peak is indicative of 'expanding' forces trying to enlarge the bilayer interfacial area. The molecular origin of the water–headgroup maxima resides in repulsive interactions of steric, electrostatic, and hydration nature [52]. Inside the headgroup region the lateral pressure drops dramatically, reaching minima of ≈ -400 atm for DMPC and ≈ -700 atm for DOPC. Such negative pressures correspond to contracting forces related to the interfacial tension; the bilayer hydrocarbon core tends to minimize its exposure to the outer hydrophilic environment. The lateral pressure troughs are related to the hydrophobic effect, which in general acts to drive hydrophobic molecules together to restrict their contact with water [31]. The pressure then rises again to positive values upon entering the hydrocarbon tail region, reaching peak magnitudes of ≈ 200 atm. The repulsive forces are here believed to be related to entropy losses; the tight packing induces the lipid tails to stretch (thus losing entropy relative to the isolated 'free' tails), ultimately leading to significant inter-tail repulsion [59].

The pressure profiles obtained with our CG model can be compared to experimental results and atomistic simulation data. Unfortunately, the experimental measurements are extremely problematic, and only qualitative and partial data can be obtained. In particular, the internal pressure of DMPC bilayers has never been probed. Regarding DOPC, there is one reported experiment [60] that yielded a qualitative picture of the lateral pressure in part of the tail region. The data indicate an overall pressure decrease going from the

headgroup–tail interface towards the bilayer centre; this picture is generally consistent with our curve. Comparative profiles for both lipid species can be found amongst the distributions obtained from atomic-level models. The DMPC pressure profile obtained atomistically by Gullingsrud *et al* [61] displays the same qualitative features observed in our curve, in terms of number and locations of peaks and troughs. There are however quantitative discrepancies regarding the magnitude of the headgroup–water peaks, which are ≈700 atm in the atomistic profile [61] against a substantially lower value of ≈200 atm in our curve. The surface tension troughs are also more pronounced in that atomistic profile [61], where they reach magnitudes of ≈1000 atm against ≈400 atm for our data. Interestingly, recent atomistic data by Griepernau and Böckmann [62] are more consistent with ours in terms of magnitude, though they somewhat differ qualitatively. In particular, that DMPC profile [62] is characterized by headgroup troughs of very similar magnitude to ours (≈400 atm); the magnitude of the central peak is also consistent with ours (≈200 atm). However, the atomic-level profile [62] features a much smaller peak at the headgroup–water interface (≈50 atm against our value of ≈200 atm) and displays an extra headgroup trough which is absent in our curve; in fact, this trough is also absent in the atomistic profile by Gullingsrud *et al* [61]. Moreover, the curve calculated by Griepernau and Böckmann [62] comprises two large peaks (≈250 atm) corresponding to the headgroup–tail interface regions, whereas in the same regions both our curve and that obtained by Gullingsrud *et al* [61] display almost negligible peaks (≈0 atm). The DMPC lateral pressure profile of our current model is somewhat different from that obtained with our original force field [8]; while the two curves are qualitatively consistent with each other, significant differences in the pressure magnitudes can be noted. In particular, the magnitude of the water–headgroup interfacial peaks in the current model is about half the original value. The headgroup troughs of the current model are also less pronounced than those observed with the original force field; the magnitude has decreased by ≈40%. Furthermore, the local maxima in the headgroup–tail interface regions have dropped from ≈200 atm to almost zero. The original and current profiles are however in quantitative agreement regarding the peak in the bilayer centre (≈200 atm). Overall, the observed magnitude decreases are necessarily related to the presence of smaller net lateral forces in the current model than in the previous one. While it is difficult to pinpoint the precise molecular origins of these differences, some hypotheses can be considered. In particular, the new model is characterized by ≈30% larger headgroup particles (in volume); the headgroup charges in the new model are therefore 'more screened' than in the old one, ultimately yielding weaker electrostatic forces. Also, the magnitude of the glycerol dipole in the current model has been reduced to a third of the original; again, the magnitude of the corresponding electrostatic forces is expected to decrease. In general, it is clear that the lateral pressure profile is very sensitive to the model parameters. Regarding DOPC, the only pressure profile previously reported has been calculated with an atomic-level model by Ollila *et al* [63]. Their curve [63]

is generally consistent with ours (figure 3), in terms of the location of the major peaks and troughs as well as in terms of magnitudes. There is however a significant difference concerning the pressure in the bilayer centre; the atomistic profile [63] features a local maximum, whereas our curve is characterized by a minimum. This discrepancy is likely to depend on the different treatment of the lipid unsaturation. Fortunately, the pressure in the bilayer centre contributes the least to the calculation of the pressure profile integral moments, as it is clear from equations (4) and (5) reported in the next section.

5.3. Curvature elastic parameters

Following the popular theory developed by Helfrich [64], we can express the surface curvature elastic energy per unit area as:

$$g = \kappa (c_1 + c_2 - c_0)^2/2 + \kappa_{\mathrm{G}} c_1 c_2 \qquad (3)$$

with κ the bending rigidity, c_1 and c_2 the (local) principal curvatures, c_0 the spontaneous (or intrinsic) curvature, and κ_{G} the Gaussian curvature modulus. The constants featuring in equation (3) are related to the first and second integral moments of the pressure profile [59]. It is most interesting to evaluate the curvature elastic parameters for a monolayer; we will therefore calculate these quantities and denote them with the superscript m. By defining the lateral pressure profile as $\pi(z) = P_{\mathrm{L}}(z) - P_{\mathrm{N}}(z)$, the first integral moment τ_1^{m} is:

$$\tau_1^{\mathrm{m}} = \int_0^h z\, \pi(z)\, \mathrm{d}z \qquad (4)$$

and the second integral moment τ_2^{m} is:

$$\tau_2^{\mathrm{m}} = \int_0^h z^2\, \pi(z)\, \mathrm{d}z \qquad (5)$$

where $z = 0$ at the centre of the bilayer and $z = h$ in the water phase [59]. In practice, we carried out the integrations over each of the two monolayers, with $z = 0$ and $\pm h$, h being half the z-dimension of the simulation region.

From the first moment (equation (4)) it is possible to calculate the spontaneous curvature as $c_0^{\mathrm{m}} = \tau_1^{\mathrm{m}}/\kappa^{\mathrm{m}}$, κ^{m} being the monolayer bending rigidity modulus. For DMPC, we obtained a value of $\tau_1^{\mathrm{m}} = +0.700 \pm 0.001\, k_{\mathrm{B}}T\, \mathrm{nm}^{-1}$. The monolayer bending rigidity modulus can be simply obtained from the bilayer modulus as $\kappa^{\mathrm{m}} = \kappa^{\mathrm{b}}/2$ [34]. Considering the value of κ^{b} previously calculated from our simulation, we eventually obtained a monolayer spontaneous curvature $c_0^{\mathrm{m}} = +0.135 \pm 0.002\, \mathrm{nm}^{-1}$. It is also possible to predict c_0^{m} using the experimental data for κ^{b} [53, 55–57]; in this case, we obtained values of c_0^{m} ranging from $+0.044$ to $+0.101\, \mathrm{nm}^{-1}$. DMPC is a bilayer-forming lipid, hence it is expected to display a low absolute value for c_0^{m}; this is consistent with our findings. Unfortunately, to our knowledge there are no direct experimental measurements for the DMPC spontaneous curvature. An indirect prediction of $\approx+0.3\, \mathrm{nm}^{-1}$ was obtained on the basis of chemical potentials from bilayer-enzyme systems [65]. The same article [65] also proposes an estimate based on a simple geometric model; however, the

reported value of $\approx +0.25$ nm^{-1} is of the opposite sign than the value (≈ -0.25 nm^{-1}) that we obtain by applying the same model (equation (14) of [65]). Regarding DOPC, we calculated from simulation a value of $\tau_1^m = -1.30 \pm 0.03\,k_BT$ nm^{-1}. From the relation $\tau_1^m = \kappa^m c_0^m$, and considering the available experimental data for κ^b [46, 47, 53] and c_0^m [66, 67], we can calculate experimental estimates for τ_1^m ranging from -0.09 to $-2.39\,k_BT$ nm^{-1}; the value obtained from our simulation falls inside this range. As for the spontaneous curvature, using the bending rigidity obtained from simulation we calculated $c_0^m = -0.087 \pm 0.003$ nm^{-1}; using instead the experimental values for the bending rigidity [46, 47, 53] we obtained a range from -0.124 to -0.138 nm^{-1}. The direct measurement of the DOPC spontaneous curvature yielded values of -0.05 nm^{-1} [66] and -0.114 nm^{-1} [67]. All these estimates are consistent with the view that DOPC is a bilayer-forming lipid, as the magnitude of c_0^m is small; they also indicate a slight tendency towards the formation of inverse phases, as the values are negative.

From the first and second moment (equations (4) and (5)) we can obtain the Gaussian curvature modulus as $\kappa_G^m = -\int_0^h (z - \xi)^2 \pi(z)\,\mathrm{d}z = 2\xi\tau_1^m - \tau_2^m$, ξ being the distance to the *pivotal surface*, defined as the surface at which there is no change in the molecular cross-sectional area upon bending [34]. The pivotal surface has been experimentally located close to the polar/apolar interface [68], corresponding to the headgroup/tail interface in our systems (figure 3). Specifically, we placed the pivotal surface as corresponding to the first maximum of the pressure profile after the headgroup trough towards the bilayer centre (as similarly done by Ollila *et al* [63]). Following this convention, our values for ξ are 0.89 nm for DMPC and 1.25 nm for DOPC. For the Gaussian curvature modulus we eventually calculated the values of $-7.2 \pm 0.1\,k_BT$ for DMPC and $-6.7 \pm 0.1\,k_BT$ for DOPC; both these results are consistent with the ranges obtained from experimental data [53, 57, 68], that is, -16 to $0\,k_BT$ for DMPC, and -10.5 to $0\,k_BT$ for DOPC.

5.4. Dipole potential

The electrostatic potential profile $\Psi(z)$ can be calculated by integrating twice the charge density ρ along the interface normal [69]:

$$\Psi(z) = -\frac{1}{\epsilon_0} \int_0^z \mathrm{d}z' \int_0^{z'} \rho(z'')\,\mathrm{d}z'' \tag{6}$$

with ϵ_0 the permittivity of free space. Figure 4 reports the total transmembrane electrostatic potentials of our models, together with individual profiles. The membrane dipole potential, taken as the difference between the potential in the hydrocarbon core with respect to that in the water phase, has been obtained experimentally with a variety of methods. Recent measurements include a value of $+0.45$ V for DMPC obtained with the monolayer method [11], a value of $+0.51$ V for a diphytanoylphosphatidylcholine (DPhPC) bilayer obtained by cryo electron microscopy [12] and a value of $+0.275$ V for DOPC obtained by atomic force microscopy [13]. These results can be considered as representative for ester–PC lipid
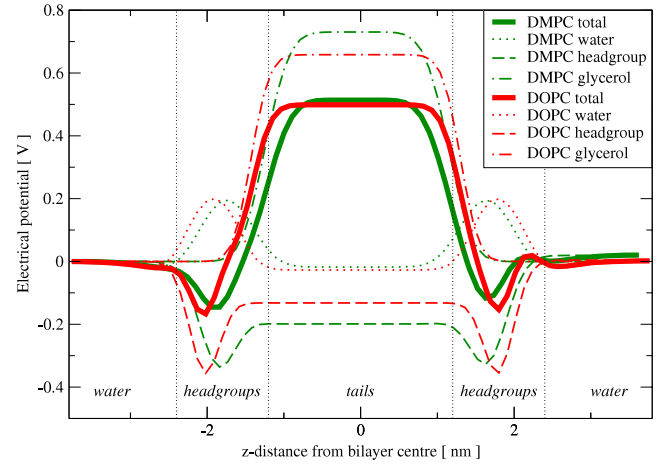
Figure 4. Electrostatic potential profiles. The total transmembrane potentials are plotted together with individual profiles.

bilayers in general, due to the presence of the same charged groups (glycerol-ester and headgroup). Our models yielded a dipole potential of $+0.514 \pm 0.002$ V for DMPC and $+0.499 \pm 0.006$ V for DOPC, in reasonable agreement with the experimental data. We also calculated the contributions to the total electrostatic potential profiles from the various charged groups; it can be seen that for both DMPC and DOPC the main contributors to the potential are the glycerol-ester dipoles, while headgroups and water play relatively minor roles (figure 4). While experimentally it has not been possible, so far, to discriminate between the different contributions to the electrostatic potential, such an analysis has been performed with atomistic models [70–73]. According to these studies, water is the leading contributor to the dipole potential; there is therefore a qualitative discrepancy with our CG model. This disagreement reflects different behaviours of the water molecules in our model and in AL systems. In particular, the large water electrostatic potential observed in AL studies derives from a pronounced and homogeneous alignment of the water dipoles interacting with the lipid headgroups. In our systems, we instead observe weaker orientational effects that prevent water from making a substantial contribution to the overall potential. Regarding the specific contribution of the glycerol region, our data are consistent with the results obtained in the all-atom simulations by Shinoda *et al* [70, 71]. However, the glycerol contribution to the overall potential is almost negligible in united-atom models [73]. In general, experimental data quantifying the various contributions to the dipole potential are currently lacking, making it difficult to critically assess the different results obtained with the various simulation models. Overall, it is important to stress that, despite possible inaccuracies regarding individual contributions, our model correctly reproduces the experimentally-determined net dipole potential. This should provide a realistic electrostatic environment for the potential inclusion of proteins in the system. In fact, it is reasonable to expect that membrane proteins would be mainly sensitive to the total net potential across the bilayer, and not so much to the specific individual contributions.

5.5. Lipid lateral diffusion

The lipid centre of mass diffusion coefficient $D(t)$ in the xy-plane has been calculated using the expression:

$$D(t) = \frac{1}{4Nt}\left\langle \sum_{i=1}^{N}[\mathbf{r}_i(t+t_0) - \mathbf{r}_i(t_0)]^2 \right\rangle \qquad (7)$$

where N is the number of lipids, t is the measurement time, t_0 is the time at which a measurement starts, and $\mathbf{r}_i(t+t_0)$ and $\mathbf{r}_i(t_0)$ are the centre of mass positions of lipid i at times $t + t_0$ and t_0. The angular brackets in equation (7) indicate an averaging over different starting times t_0. For both the DMPC and the DOPC simulation systems, we selected 10 starting times $t_0 = 0, 20, 40, \ldots, 180$ ns and carried out 10 corresponding diffusion measurements for t extending to 1 μs; figure 5 displays the averaged lateral diffusion coefficients obtained. The initial spike accounts for fast 'rattling-like' diffusion taking place over very short measurement times, approximately for $t < 10$ ns. Subsequently, for intermediate times, up to $t \approx 0.2$ μs, we observe a drop in diffusion values, as the 'rattling' motion yields much decreased net displacements over this timescale. Over longer times, the diffusion coefficients converge to stable values. In particular, for $t = 1$ μs we calculate diffusion coefficients of 10.6 ± 0.3 nm^2 μs^{-1} for DMPC and 11.7 ± 0.2 nm^2 μs^{-1} for DOPC. Experimentally, measurements on DMPC yielded diffusion coefficients of 9 nm^2 μs^{-1} from NMR [74], 6 nm^2 μs^{-1} from fluorescence recovery after photobleaching [75] and 40 nm^2 μs^{-1} from high-frequency dielectric spectroscopy [76]. Regarding DOPC, a value of 11.5 nm^2 μs^{-1} was obtained by NMR [74]. Overall, the results obtained with our CG model are in remarkably good agreement with the experimental data. This represents an improvement over alternative CG models developed to date, for which lipid diffusion coefficients have been reported to be four [7, 77] to one hundred [78] times higher than experimental data. In fact, CG models are generally expected to exhibit faster dynamics with respect to AL counterparts, because the reduction in the number of degrees of freedom normally results in reduced friction in the system [79]. However, our CG model does not seem to be affected by such a 'speed-up' effect, at least for the lipid diffusion process. The direct correlation between fewer degrees of freedom and faster dynamics is also inconsistent with water simulation results reported by Fennel and Gezelter [28]. That study compares the diffusion coefficients of one-site, three-site and five-site water models. At physiological temperatures, the largest diffusion coefficient was obtained for the five-site model [28]. These apparent contradictions can be explained by considering that other factors might compensate for the loss of friction. For example, the CG non-bonded interactions can subtly differ from those in corresponding AL systems; in particular, if the CG intermolecular interactions prove overall more attractive, this might reintroduce the friction lost in the reduction of degrees of freedom.
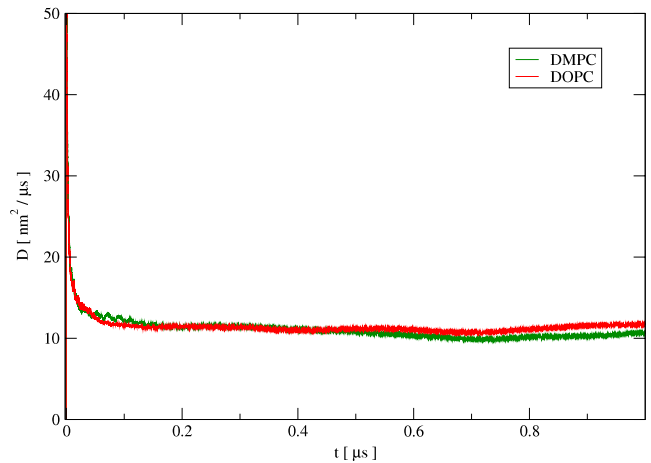

Figure 5. Lateral diffusion coefficients of lipid mass centres calculated using the Einstein relation as a function of the measurement time.

We also obtained qualitative insights into the lipid lateral diffusion process by tracking the mass centre motion of individual lipids over the entire 1.2 μs runs; typical examples are displayed in figure 6. The lipid diffusion mechanism has been often described through the free-volume theory [80]. According to this model, lipids spend most of their time rattling around fixed locations; net displacements take place through occasional 'jumps' of lipid molecules into nearby vacancies formed by lateral density fluctuations. The lipid traces extracted from our simulations are only partially consistent with the free-volume model. While it is evident that lipids do not diffuse through continuous flowing, it is also difficult to identify discrete jumping events. Our data show that lipids do mainly rattle around fixed spots. However, such spots are not connected by well-defined jumps; rather, lipids seem to slowly rattle from one spot to the next. The jump–diffusion model has also been recently challenged by Falck *et al* [81]; in fact, their atomistic simulations yielded lipid diffusive patterns similar to those obtained with our model. Unfortunately, there are no experimental data directly showing the diffusive mechanism at this level of resolution.

5.6. Water permeation

The relatively long time period sampled by the coarse-grain simulations allowed us to record statistically significant numbers of water molecules crossing the bilayers from one water phase to the other; during each of the 1.2 μs simulations, we recorded 161 water molecules translocating across the DMPC bilayer and 136 water molecules translocating across the DOPC bilayer. The water permeability coefficients could then be simply obtained by applying Fick's first law of diffusion, as done previously [8]. In particular, for each system, we calculated the average and standard error by considering the two (independent) estimates deriving from the two opposite water fluxes across the bilayer, that is, the flux along the positive z-axis direction and that along the opposite (negative) z-axis direction. For DMPC, we obtained a permeability coefficient of 52 ± 2 μm s^{-1}, in remarkable
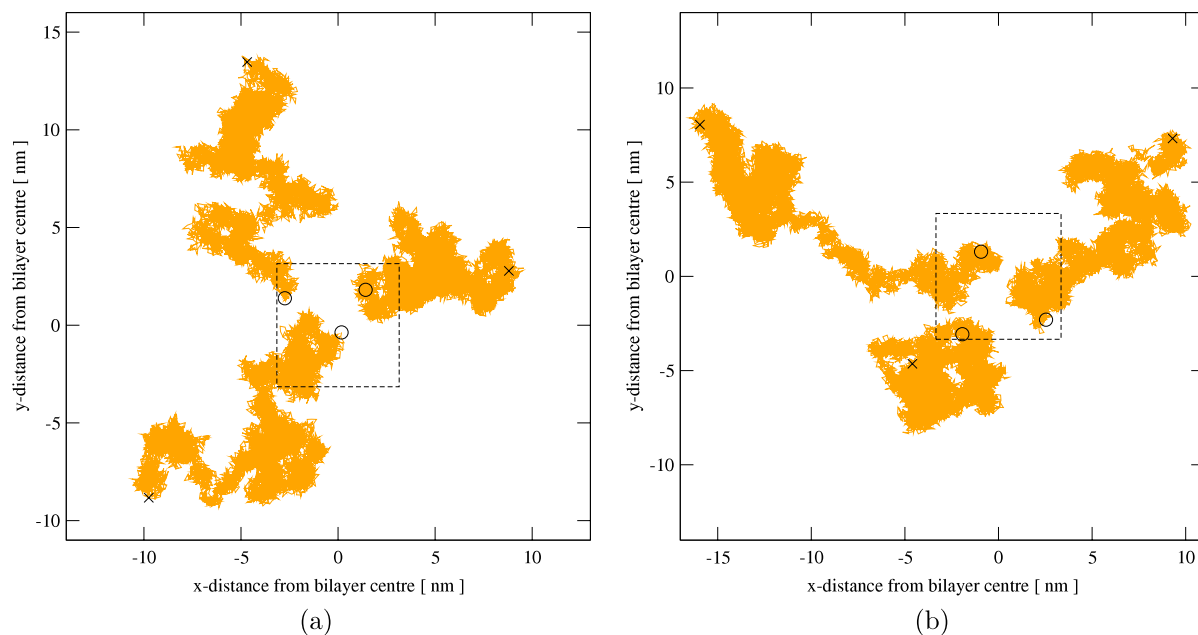
Figure 6. Single lipid lateral traces from the DMPC system (a) and the DOPC system (b). Each trace corresponds to the mass centre trajectory of a single lipid projected onto the xy plane. Initial lipid positions are marked with 'O' symbols, final positions (after 1.2 μs) with '×' symbols. The x and y lateral edges of the (central) simulation cell are represented by dashed lines.
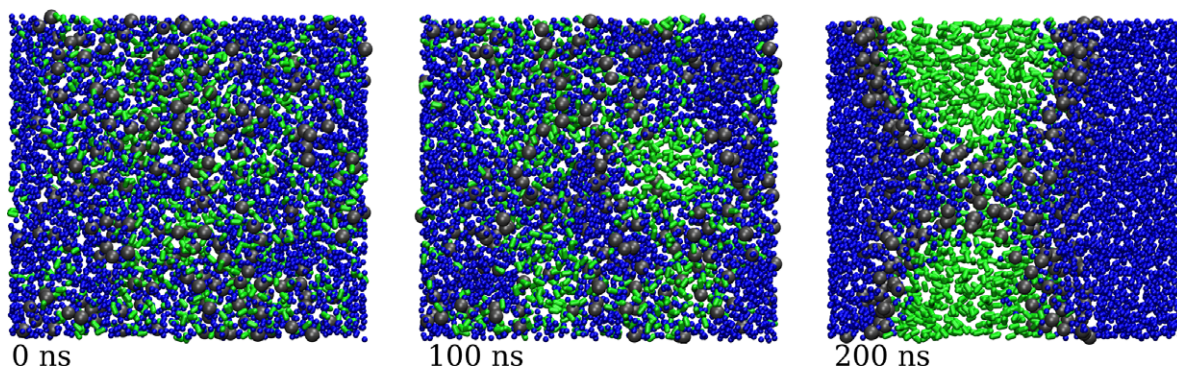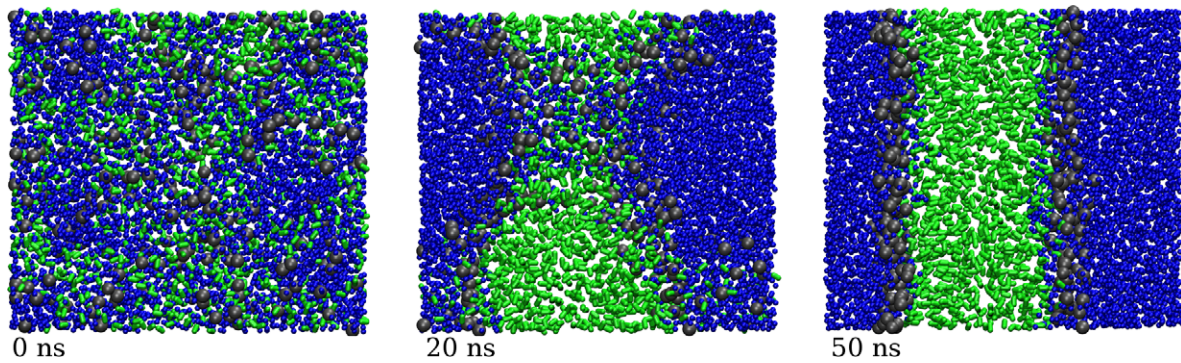

Figure 7. DMPC self-assembly simulation snapshots. The headgroups, tails and water are represented in grey, green and blue, respectively.

agreement with the experimental measurements, which span a range from 4 to 240 μm s^{-1} [82–86]. Recently, we also used our DMPC model to calculate the water permeability coefficient in an indirect way, that is, not by simulating the phenomenon directly but through the application of constraints [87]; the value of 14 μm s^{-1} obtained in that study [87] is comparable with the result obtained here. For DOPC, we obtained a permeability coefficient of 38 $\pm$ 1 μm s^{-1}, slightly lower than the experimental measurements of 56, 122 and 158 μm s^{-1} [88–90]. It is important to note that spontaneous water transport has never been quantified with atomic-level models, due to the very demanding computational efforts required to simulate long enough trajectories. For example, in a recent state-of-the-art atomistic study [91], four phosphatidylcholine bilayers, each comprising 128 lipids, were simulated for 50 ns. In the four simulations, only 2, 4, 6 and 7 crossing events were respectively observed; an estimation

of the permeability coefficient on the basis of such limited statistics would not be reliable.

5.7. Self-assembly

The ability of the DMPC and DOPC models to spontaneously self-assemble was tested by running six simulations (three for each lipid species) starting from random mixtures. The same simulation protocol and system sizes described previously were adopted. Interestingly, the two lipids behaved differently. Snapshots from a representative DMPC simulation are reported in figure 7. The system remained in a random state for several tens of ns. At $\approx$100 ns, the formation of lipid aggregates can be noticed (central panel of figure 7). At $\approx$200 ns, the system assembled in a bilayer containing a water pore. The pore remained stable until the end of the run at $\approx$500 ns. Similar events and timescales were observed for all three DMPC

Figure 8. DOPC self-assembly simulation snapshots. The headgroups, tails and water are represented in grey, green and blue, respectively.

runs. Snapshots from a representative DOPC simulation are displayed in figure 8. In this case, we can observe a fast phase separation, the formation of a transient water pore and eventually the stabilization of a fully-formed bilayer at ≈ 50 ns; again, similar patterns recurred in all three simulations involving this lipid type.

We believe that the different behaviours observed are determined by the different spontaneous curvatures of the two lipids. From the simulation data, we obtained a DMPC spontaneous curvature estimate of $c_0^m = 0.135$ nm^{-1}. For DOPC, the spontaneous curvature was instead $c_0^m = -0.087$ nm^{-1}. In absolute terms, the DMPC spontaneous curvature is therefore $\approx 55\%$ larger than DOPC's. Since the formation of a bilayer structure is more favoured the lower the absolute value of the spontaneous curvature [31], we expect our DOPC model to have a higher tendency towards bilayer structures than DMPC, in agreement with the observations from the self-assembly tests. It is relevant to note that our original DMPC model [8], which was characterized by a low absolute spontaneous curvature (0.018 nm^{-1}), was indeed observed to self-assemble into defect-free bilayers over timescales of ≈ 100 ns. We also note that the positive and non-negligible value obtained for the spontaneous curvature of the current DMPC model is consistent with a tendency of the lipids to bend away from the water phase [31], as in fact observed in the DMPC runs; for example, the water pore shown in the rightmost panel in figure 7 allows lipids to adopt a positive curvature. It is not easy to establish whether the observed DMPC pore-containing bilayer represents a "final" stable structure, or rather a metastable intermediate that would eventually reorganize into a defect-free bilayer if simulated for longer times. In fact, electroporation experiments suggest that transient pores can remain stable over milliseconds, occasionally even reaching lifetimes up to ≈ 1 s, before disappearing into a defect-free membrane [92, 93]; unfortunately, these timescales are not accessible by simulation. We also note that the preassembled DMPC bilayer that we simulated for 1.2 μs proved stable, as shown by the results presented in the previous sections.

6. Conclusion and outlook

The refinement of a coarse-grain model for DMPC lipids, and its transfer to DOPC (one of the more typical lipid species in real cell membranes), have been reported. The models have been fine-tuned to reproduce the most fundamental biophysical properties of lipid bilayers, including the spontaneous curvature and the dipole potential. Our coarse-grain technique is unique in its consistent description of the system electrostatics, especially with respect to water and the lipid glycerol-ester region; these features are essential to describe the membrane electrostatic potential, which in fact has never been studied by alternative coarse-grain models. The most fundamental membrane physical properties have been calculated from microsecond-long simulations; our results compare generally well with the available experimental data. In particular, we obtained remarkably realistic results for properties not parametrized for, such as lipid diffusion and spontaneous water permeation.

Future extensions will involve the modelling of lipids forming inverse phases, such as phosphatidylethanolamine (PE) lipids. Since the force field was here parametrized concurrently for DMPC and DOPC, we expect transferability to be facilitated, with most parameters retaining their validity across lipid types.

Moreover, the unique features of our coarse-grain technique allowed the direct incorporation of standard atomistic representations of small molecules [87, 94]; such a dual-resolution approach has also been recently applied to study the interaction of membranes with drugs, hormones and antimicrobial molecules (manuscripts in preparation). Future work in this area will involve the simulation of membrane proteins.

Acknowledgment

Appendix A. Angular potential, forces and torques

We present here the derivation of forces and torques between two sites interacting through the angular potential that we use
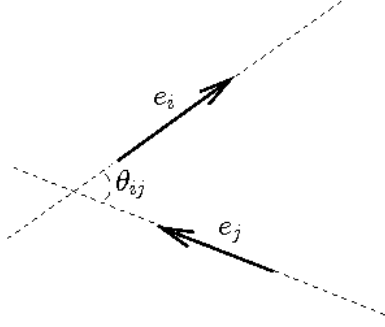
Figure A.1. Schematics of the vectors and angle characterizing the angular potential.

to represent unsaturations in the CG lipid model. Figure A.1 depicts a general configuration for a pair of linearly symmetric rigid bodies (e.g., Gay–Berne ellipsoids) whose orientations are defined by the two vectors $\mathbf{e}_i$ and $\mathbf{e}_j$.

Considering the angle θ_{ij} between the two orientation vectors, we define the angular potential u_{ij} as follows:

$$u_{ij} = \frac{k_{\theta_{ij}}}{2}(\cos\theta_{ij} - \cos\theta_0)^2 = \frac{k_{\theta_{ij}}}{2}(\mathbf{e}_i \cdot \mathbf{e}_j - \cos\theta_0)^2 \quad (A.1)$$

with k_θ the rigidity constant and θ_0 the reference angle. The interaction force is in general obtained from the gradient of the potential with respect to the separation vector. Since in this case the potential does not depend on the separation vector, the interaction force is zero:

$$\mathbf{f}_{ij} = -\nabla_{\mathbf{r}_{ij}} u_{ij} = 0. \quad (A.2)$$

The torque on site i due to site j is defined by:

$$\mathbf{T}_{ij} = -\mathbf{e}_i \times \nabla_{\mathbf{e}_i} u_{ij}. \quad (A.3)$$

Applying the chain rule, we can write:

$$\nabla_{\mathbf{e}_i} u_{ij} = \left(\frac{\partial u_{ij}}{\partial \cos\theta_{ij}}\right) \nabla_{\mathbf{e}_i} \cos\theta_{ij}. \quad (A.4)$$

Solving the derivatives, we obtain:

$$\left(\frac{\partial u_{ij}}{\partial \cos\theta_{ij}}\right) = -k_{\theta_{ij}}(\cos\theta_{ij} - \cos\theta_0)\sin\theta_{ij} \quad (A.5)$$

$$\nabla_{\mathbf{e}_i} \cos\theta_{ij} = \nabla_{\mathbf{e}_i}(\mathbf{e}_i \cdot \mathbf{e}_j) = \mathbf{e}_j. \quad (A.6)$$

The final expression is therefore:

$$\mathbf{T}_{ij} = k_{\theta_{ij}}(\cos\theta_{ij} - \cos\theta_0)\sin\theta_{ij}(\mathbf{e}_i \times \mathbf{e}_j). \quad (A.7)$$

Also, we can write:

$$\mathbf{T}_{ji} = \mathbf{T}_{ij} \quad (A.8)$$

due to symmetry.

Appendix B. Force field parameters

The parameter set for our CG force field is reported in table B.1.

Table B.1. Force field parameters. (Note: Subscripts C, P, G, T and W stand for the site types choline, phosphate, glycerol, tail and water, respectively. Lennard-Jones cross terms are calculated by a standard rule [42] except for ϵ_{TW}, ϵ_{TC}, ϵ_{TP}, ϵ_{WP}, ϵ_{WG}, ϵ_{CG}, which are set as reported in the table. The constants μ, ν, κ and κ' refer to Gay–Berne parameters [32]. As for the mixed Gay–Berne/Lennard-Jones potential [95], cross terms $\chi\alpha^{-2}$ are calculated by a standard rule [95], and $\chi'\alpha'^{-2} = 0$. Charges and dipoles are identified by Q and μ; cross terms are obtained via standard electrostatic formulae [96]. The rigidity of the Hooke spring potential is identified by k; reference lengths are zero. Springs are anchored at the mass centre for C and P sites, and at a distance $\kappa\sigma_{TT}/4$ from the mass centre along the symmetry axes for G and T sites. The parameters $k_{\theta_{ij}}$ and θ_0 characterize the angular potential modelling the DOPC unsaturation. Masses and principal moments of inertia are identified by m and I, respectively.)

Parameter	Value
σ_{CC}, σ_{PP}	5.4 Å
σ_{GG}, σ_{TT}	3.6 Å
σ_{WW}	3.035 Å
ϵ_{CC}, ϵ_{PP}	2.0 kcal mol^{-1}
ϵ_{GG}, ϵ_{TT}	1.4 kcal mol^{-1}
ϵ_{WW}	0.152 kcal mol^{-1}
ϵ_{TW}	$\sqrt{\epsilon_{TT}\,\epsilon_{WW}}/5$
ϵ_{TC}	$\sqrt{\epsilon_{TT}\,\epsilon_{CC}}/5$
ϵ_{TP}	$\sqrt{\epsilon_{TP}\,\epsilon_{PP}}/5$
ϵ_{WP}	$1.5\sqrt{\epsilon_{WW}\,\epsilon_{PP}}$
ϵ_{WG}	$1.5\sqrt{\epsilon_{WW}\,\epsilon_{GG}}$
ϵ_{CG}	$\sqrt{\epsilon_{CC}\,\epsilon_{GG}}/1.2$
μ	2
ν	1
κ	1.8
κ'	20
Q_C	$+0.7e$
Q_P	$-0.7e$
μ_G	1 D
μ_W	2.42 D
k	2 kcal (mol^{-1} Å^{-2})
$k_{\theta_{ij}}$	50 kcal mol^{-1}
θ_0	120°
m_C	73 amu
m_P	109 amu
m_G	65 amu
m_T	56 amu
m_W	50 amu
I_G	179 amu Å^2
I_T	154 amu Å^2
$[I_W^x \ I_W^y \ I_W^z]$	[25 8 17] amu Å^2

Appendix C. Tabulated results

The CG simulation results obtained for DMPC and DOPC are collected in tables C.1 and C.2, respectively, together with corresponding experimental measurements.

12

Table C.1. Physical parameters of fluid-phase DMPC phospholipid bilayer.

Parameter[a]	Our model	Experiment (reference)
V_L (nm^3)	1.0917 ± 0.0001	1.101 [43]
A_L (Å^2)	61.59 ± 0.04	60.6 [43], 59.7 [44]
d_{HH} (nm)	3.467 ± 0.003	3.53 [43]
μ_{HG} (D)	17.7935 ± 0.0001	18.7 [54][b]
θ_{HG} (deg)	88.90 ± 0.01	$\approx$72 [38][b]
K_V (kbar)	12.43 ± 0.02	10 to 30 [52]
K_A (dyn cm^{-1})	166 ± 22	234 [53]
κ^b ($k_B T$)	10.4 ± 0.3	13.8 [53], 16.7 [55], 31.4 [56], 32.1 [57]
τ_1^m ($k_B T$ nm^{-1})	$+0.700 \pm 0.001$	Not available
c_0^m (nm^{-1})	$+0.135 \pm 0.002$[c]	Not available
c_0^m (nm^{-1})	$+0.044$ to $+0.101$[d]	Not available
κ_G^m ($k_B T$)	-7.2 ± 0.1	-16 to 0 [57, 68]
Ψ_d (V)	$+0.514 \pm 0.002$	$+0.45$ [11], $+0.51$ [12][e]
D_{lat} (nm^2 μs^{-1})	10.6 ± 0.3	9 [74], 6 [75], 40 [76]
P_W (μm s^{-1})	52 ± 2	4 [83], 6 [82], 10 [83], 70 [84], 83 [85], 240 [86]

[a] Abbreviations: V_L = volume per lipid, A_L = area per lipid, d_{HH} = bilayer thickness, μ_{HG} = magnitude of the headgroup dipole, θ_{HG} = angle between the headgroup dipole and the bilayer normal, K_A = area compressibility, K_V = volume compressibility, κ^b = bilayer bending rigidity, τ_1^m = first integral moment of the pressure profile, c_0^m = monolayer spontaneous curvature, κ_G^m = monolayer Gaussian curvature, κ_G^b = bilayer Gaussian curvature, Ψ_d = dipole potential, D_{lat} = lipid lateral diffusion, P_W = water permeability.
[b] Fluid-phase DPPC. [c] Obtained using κ^b from simulation. [d] Obtained using κ^b from experiments. [e] Fluid-phase DPhPC.

Table C.2. Physical parameters of fluid-phase DOPC phospholipid bilayer.

Parameter[a]	Our model	Experiment (reference)
V_L (nm^3)	1.3057 ± 0.0001	1.303 [46]
A_L (Å^2)	69.54 ± 0.15	67.4 [45], 72.1 [47], 72.2 [50], 72.4 [46], 72.5 [51]
d_{HH} (nm)	3.820 ± 0.008	3.53 [50], 3.67 [46], 3.71 [47]
μ_{HG} (D)	17.7984 ± 0.0001	18.7 [54][b]
θ_{HG} (deg)	89.21 ± 0.04	$\approx$72 [38][b]
K_V (kbar)	12.84 ± 0.04	10 to 30 [52]
K_A (dyn cm^{-1})	366 ± 9	188 [50], 265 [53]
κ^b ($k_B T$)	30.0 ± 1.0	18.8 [46], 19.8 [47], 21.0 [53]
τ_1^m ($k_B T$ nm^{-1})	-1.30 ± 0.03	-0.09 to -2.39 [46, 53, 66, 67]
c_0^m (nm^{-1})	-0.087 ± 0.003[c]	-0.05 [66], -0.114 [67]
c_0^m (nm^{-1})	-0.124 to -0.138[d]	-0.05 [66], -0.114 [67]
κ_G^m ($k_B T$)	-6.7 ± 0.1	-10.5 to 0 [53, 68]
Ψ_d (V)	$+0.499 \pm 0.006$	$+0.275$ [13], $+0.51$ [12][e]
D_{lat} (nm^2 μs^{-1})	11.7 ± 0.2	11.5 [74]
P_W (μm s^{-1})	38 ± 1	56 [88], 122 [89], 158 [90]

[a] Abbreviations: V_L = volume per lipid, A_L = area per lipid, d_{HH} = bilayer thickness, μ_{HG} = magnitude of the headgroup dipole, θ_{HG} = angle between the headgroup dipole and the bilayer normal, K_A = area compressibility, K_V = volume compressibility, κ^b = bilayer bending rigidity, τ_1^m = first integral moment of the pressure profile, c_0^m = monolayer spontaneous curvature, κ_G^m = monolayer Gaussian curvature, κ_G^b = bilayer Gaussian curvature, Ψ_d = dipole potential, D_{lat} = lipid lateral diffusion, P_W = water permeability. [b] Fluid-phase DPPC. [c] Obtained using κ^b from simulation. [d] Obtained using κ^b from experiments. [e] Fluid-phase DPhPC.

References

[1] Muller M, Katsov K and Schick M 2006 Biological and synthetic membranes: what can be learned from a coarse-grained description? *Phys. Rep.* **434** 113–76

[2] Brannigan G, Lin L C L and Brown F L H 2006 Implicit solvent simulation models for biomembranes *Eur. Biophys. J.* **35** 104–24

[3] Orsi M, Sanderson W and Essex J W 2007 Coarse-grain modelling of lipid bilayers: a literature review *Molecular Interactions—Bringing Chemistry to Life* ed M G Hicks and C Kettner (Frankfurt: Beilstein-Institut) pp 185–205

[4] Shelley J C, Shelley M Y, Reeder R C, Bandyopadhyay S and Klein M L 2001 A coarse grain model for phospholipid simulations *J. Phys. Chem.* B **105** 4464–70

[5] Kranenburg M, Nicolas J P and Smit B 2004 Comparison of mesoscopic phospholipid–water models *Phys. Chem. Chem. Phys.* **6** 4142–51

[6] Izvekov S and Voth G A 2005 A multiscale coarse-graining method for biomolecular systems *J. Phys. Chem.* B **109** 2469–73

[7] Marrink S-J, Risselada H J, Yefimov S, Tieleman D P and de Vries A H 2007 The MARTINI force field: coarse

grained model for biomolecular simulations *J. Phys. Chem.* B **111** 7812–24

[8] Orsi M, Haubertin D Y, Sanderson W E and Essex J W 2008 A quantitative coarse-grain model for lipid bilayers *J. Phys. Chem.* B **112** 802–15

[9] Winger M, Trzesniak D, Baron R and van Gunsteren W F 2009 On using a too large integration time step in molecular dynamics simulations of coarse-grained molecular models *Phys. Chem. Chem. Phys.* **11** 1934–41

[10] Clarke R J 2001 The dipole potential of phospholipid membranes and methods for its detection *Adv. Colloid Interface Sci.* **89** 263–81

[11] Lairion F and Disalvo E A 2004 Effect of phloretin on the dipole potential of phosphatidylcholine, phosphatidylethanolamine, and phosphatidylglycerol monolayers *Langmuir* **20** 9151–5

[12] Wang L, Bose P S and Sigworth F J 2006 Using cryo-EM to measure the dipole potential of a lipid membrane *Proc. Natl Acad. Sci. USA* **103** 18528–33

[13] Yang Y, Mayer K M, Wickremasinghe N S and Hafner J H 2008 Probing the lipid membrane dipole potential by atomic force microscopy *Biophys. J.* **95** 5193–9

[14] Cladera J, Martin I and O'Shea P 2001 The fusion domain of HIV gp41 interacts specifically with heparan sulfate on the t-lymphocyte cell surface *Embo J.* **20** 19–26

[15] Franklin J C and Cafiso D S 1993 Internal electrostatic potentials in bilayers—measuring and controlling dipole potentials in lipid vesicles *Biophys. J.* **65** 289–99

[16] Starke-Peterkovic T, Turner N, Else P L and Clarke R J 2005 Electric field strength of membrane lipids from vertebrate species: membrane lipid composition and Na$^+$-K$^+$-ATPase molecular activity *Am. J. Physiol. Regul. Integr. Comp. Physiol.* **288** R663–70

[17] Rokitskaya T I, Kotova E A and Antonenko Y N 2002 Membrane dipole potential modulates proton conductance through gramicidin channel: movement of negative ionic defects inside the channel *Biophys. J.* **82** 865–73

[18] Maggio B 1999 Modulation of phospholipase A_2 by electrostatic fields and dipole potential of glycosphingolipids in monolayers *J. Lipid Res.* **40** 930–9

[19] Cladera J and O'Shea P 1998 Intramembrane molecular dipoles affect the membrane insertion and folding of a model amphiphilic peptide *Biophys. J.* **74** 2434–42

[20] Gelbart W M, Bruinsma R F, Pincus P A and Parsegian V A 2000 DNA-inspired electrostatics *Phys. Today* **53** 38–44

[21] Alakoskela J-M I and Kinnunen P K J 2001 Control of a redox reaction on lipid bilayer surfaces by membrane dipole potential *Biophys. J.* **80** 294–304

[22] Cladera J, O'Shea P, Hadgraft J and Valenta C 2003 Influence of molecular dipoles on human skin permeability: use of 6-ketocholestanol to enhance the transdermal delivery of bacitracin *J. Pharm. Sci.* **92** 1018–27

[23] Cafiso D S 1998 Dipole potentials and spontaneous curvature: membrane properties that could mediate anesthesia *Toxicol. Lett.* **101** 431–9

[24] Asawakarn T, Cladera J and O'Shea P 2001 Effects of the membrane dipole potential on the interaction of saquinavir with phospholipid membranes and plasma membrane receptors of Caco-2 cells *J. Biol. Chem.* **276** 38457–63

[25] O'Shea P 2003 Intermolecular interactions with/within cell membranes and the trinity of membrane potentials: kinetics and imaging *Biochem. Soc. Trans.* **31** 990–6

[26] Liu Y and Ichiye T 1996 Soft sticky dipole potential for liquid water *J. Phys. Chem.* **100** 2723–9

[27] Chandra A and Ichiye T 1999 Dynamical properties of the soft sticky dipole model of water: molecular dynamics simulations *J. Chem. Phys.* **111** 2701–9

[28] Fennell C J and Gezelter J D 2004 On the structural and transport properties of the soft sticky dipole and related single-point water models *J. Chem. Phys.* **120** 9175–84

[29] Tan M-L, Brooks B R and Ichiye T 2006 Temperature dependence of diffusion properties of soft sticky dipole water *Chem. Phys. Lett.* **421** 166–70

[30] Voet D and Voet J G 2004 *Biochemistry* 3rd edn (New York: Wiley)

[31] Mouritsen O G 2005 *Life—As a Matter of Fat. The Emerging Science of Lipidomics* 1st edn (Berlin: Springer)

[32] Gay J G and Berne B J 1981 Modification of the overlap potential to mimic a linear site-site potential *J. Chem. Phys.* **74** 3316–9

[33] Whitehead L, Edge C M and Essex J W 2001 Molecular dynamics simulation of the hydrocarbon region of a biomembrane using a reduced representation model *J. Comput. Chem.* **22** 1622–33

[34] Shearman G C, Ces O, Templer R H and Seddon J M 2006 Inverse lyotropic phases of lipids and membrane curvature *J. Phys.: Condens. Matter* **18** S1105–24

[35] Bezrukov S M 2000 Functional consequences of lipid packing stress *Curr. Opin. Colloid Interface Sci.* **5** 237–43

[36] Attard G S, Templer R H, Smith W S, Hunt A N and Jackowski S 2000 Modulation of CTP: phosphocholine cytidylyltransferase by membrane curvature elastic stress *Proc. Natl Acad. Sci. USA* **97** 9032–6

[37] Botelho A V, Huber T, Sakmar T P and Brown M F 2006 Curvature and hydrophobic forces drive oligomerization and modulate activity of rhodopsin in membranes *Biophys. J.* **91** 4464–77

[38] Akutsu H and Nagamori T 1991 Conformational analysis of the polar head group in phosphatidylcholine bilayers: a structural change induced by cations *Biochemistry* **30** 4510–6

[39] *BRAHMS: a Biomembrane Reduced-ApproacH Molecular Simulator* http://www.personal.soton.ac.uk/orsi/brahms/

[40] Dullweber A, Leimkuhler B and McLachlan R 1997 Symplectic splitting methods for rigid body molecular dynamics *J. Chem. Phys.* **107** 5840–51

[41] Berendsen H J C, Postma J P M, van Gunsteren W F, Di Nola A and Haak J R 1984 Molecular dynamics with coupling to an external bath *J. Chem. Phys.* **81** 3684–90

[42] Allen M P and Tildesley D J 1987 *Computer Simulation of Liquids* 1st edn (Oxford: Oxford Science Publications)

[43] Kučerka N, Liu Y F, Chu N J, Petrache H I, Tristram-Nagle S T and Nagle J F 2005 Structure of fully hydrated fluid phase DMPC and DLPC lipid bilayers using x-ray scattering from oriented multilamellar arrays and from unilamellar vesicles *Biophys. J.* **88** 2626–37

[44] Petrache H I, Tristram-Nagle S and Nagle J F 1998 Fluid phase structure of EPC and DMPC bilayers *Chem. Phys. Lipids* **95** 83–94

[45] Kučerka N, Nagle J F, Sachs J N, Feller S E, Pencer J, Jackson A and Katsaras J 2008 Lipid bilayer structure determined by the simultaneous analysis of neutron and x-ray scattering data *Biophys. J.* **95** 2356–67

[46] Pan J, Tristram-Nagle S, Kučerka N and Nagle J F 2008 Temperature dependence of structure, bending rigidity, and bilayer interactions of dioleoylphosphatidylcholine bilayers *Biophys. J.* **94** 117–24

[47] Liu Y F and Nagle J F 2004 Diffuse scattering provides material parameters and electron density profiles of biomembranes *Phys. Rev.* E **69** 040901

[48] Högberg C-J and Lyubartsev A P 2006 A molecular dynamics investigation of the influence of hydration and temperature on structural and dynamical properties of a dimyristoylphosphatidylcholine bilayer *J. Phys. Chem.* B **110** 14326–36

[49] Klauda J B, Kučerka N, Brooks B R, Pastor R W and Nagle J F 2006 Simulation-based methods for interpreting x-ray data from lipid bilayers *Biophys. J.* **90** 2796–807

[50] Tristram-Nagle S, Petrache H I and Nagle J F 1998 Structure and interactions of fully hydrated dioleoylphosphatidylcholine bilayers *Biophys. J.* **75** 917–25

[51] Nagle J F and Tristram-Nagle S 2000 Structure of lipid bilayers *Biochim. Biophys. Acta* **1469** 159–95

[52] Cevc G and Marsh D 1987 *Phospholipid Bilayers—Physical Principles and Models* 1st edn (New York: Wiley)

[53] Rawicz W, Olbrich K C, McIntosh T, Needham D and Evans E 2000 Effect of chain length and unsaturation on elasticity of lipid bilayers *Biophys. J.* **79** 328–39

[54] Shepherd J C W and Büldt G 1978 Zwitterionic dipoles as a dielectric probe for investigating head group mobility in phospholipid membranes *Biochim. Biophys. Acta* **514** 83–94

[55] Chu N, Kučerka N, Liu Y F, Tristram-Nagle S and Nagle J F 2005 Anomalous swelling of lipid bilayer stacks is caused by softening of the bending modulus *Phys. Rev.* E **71** 041904

[56] Méléard P, Gerbeaud C, Pott T, Fernandez-Puente L, Bivas I, Mitov M D, Dufourcq J and Bothorel P 1997 Bending elasticities of model membranes: influences of temperature and sterol content *Biophys. J.* **72** 2616–29

[57] Lee C-H, Lin W-C and Wang J 2001 All-optical measurements of the bending rigidity of lipid-vesicle membranes across structural phase transitions *Phys. Rev.* E **6402** 020901

[58] Harasima A 1958 Molecular theory of surface tension *Adv. Chem. Phys.* **1** 203–37

[59] Ben-Shaul A 1995 Molecular theory of chain packing, elasticity and lipid–protein interaction in lipid bilayers *Structure and Dynamics of Membranes* ed R Lipowsky and E Sackmann (Amsterdam: Elsevier) pp 359–401

[60] Templer R H, Castle S J, Curran A R, Rumbles G and Klug D R 1998 Sensing isothermal changes in the lateral pressure in model membranes using di-pyrenyl phosphatidylcholine *Faraday Discuss.* **111** 41–53

[61] Gullingsrud J, Babakhani A and McCammon J A 2006 Computational investigation of pressure profiles in lipid bilayers with embedded proteins *Mol. Simulat.* **32** 831–8

[62] Griepernau B and Böckmann R A 2008 The influence of 1-alkanols and external pressure on the lateral pressure profiles of lipid bilayers *Biophys. J.* **95** 5766–78

[63] Ollila O H S, Róg T, Karttunen M and Vattulainen I 2007 Role of sterol type on lateral pressure profiles of lipid membranes affecting membrane protein functionality: comparison between cholesterol, desmosterol, 7-dehydrocholesterol and ketosterol *J. Struct. Biol.* **159** 311–23

[64] Seddon J M and Templer R H 1995 Polymorphism of lipid–water systems *Structure and Dynamics of Membranes* ed R Lipowsky and E Sackmann (Amsterdam: Elsevier) pp 97–160

[65] Marsh D 2007 Lateral pressure profile, spontaneous curvature frustration, and the incorporation and conformation of proteins in membranes *Biophys. J.* **93** 3884–99

[66] Szule J A, Fuller N L and Rand R P 2002 The effects of acyl chain length and saturation of diacylglycerols and phosphatidylcholines on membrane monolayer curvature *Biophys. J.* **83** 977–84

[67] Chen Z and Rand R P 1997 The influence of cholesterol on phospholipid membrane curvature and bending elasticity *Biophys. J.* **73** 267–76

[68] Templer R H, Khoo B J and Seddon J M 1998 Gaussian curvature modulus of an amphiphilic monolayer *Langmuir* **14** 7427–34

[69] Sokhan V P and Tildesley D J 1997 The free surface of water: molecular orientation, surface potential and nonlinear susceptibility *Mol. Phys.* **92** 625–40

[70] Shinoda W, Shimizu M and Okazaki S 2008 Molecular dynamics study on electrostatic properties of a lipid bilayer: polarization, electrostatic potential, and the effects on structure and dynamics of water near the interface *J. Phys. Chem.* B **102** 6647–54

[71] Shinoda K, Shinoda W, Baba T and Mikami M 2004 Comparative molecular dynamics study of ether- and ester-linked phospholipid bilayers *J. Chem. Phys.* **121** 9648–54

[72] Cordomi A, Edholm O and Perez J J 2008 Effect of ions on a dipalmitoyl phosphatidylcholine bilayer. A molecular dynamics simulation study *J. Phys. Chem.* B **112** 1397–408

[73] Högberg C-J and Lyubartsev A P 2008 Effect of local anesthetic lidocaine on electrostatic properties of a lipid bilayer *Biophys. J.* **94** 525–31

[74] Filippov A, Orädd G and Lindblom G 2003 Influence of cholesterol and water content on phospholipid lateral diffusion in bilayers *Langmuir* **19** 6397–400

[75] Almeida P F F, Vaz W L C and Thompson T E 1992 Lateral diffusion in the liquid phases of dimyristoylphosphatidylcholine/cholesterol lipid bilayers: a free volume analysis *Biochemistry* **31** 6739–47

[76] Haibel A, Nimtz G, Pelster R and Jaggi R 1998 Translational diffusion in phospholipid bilayer membranes *Phys. Rev.* E **57** 4838–41

[77] Izvekov S and Voth G A 2006 Multiscale coarse-graining of mixed phospholipid/cholesterol bilayers *J. Chem. Theory Comput.* **2** 637–48

[78] Lopez C F, Moore P B, Shelley J C, Shelley M Y and Klein M L 2002 Computer simulation studies of biomembranes using a coarse grain model *Comput. Phys. Commun.* **147** 1–6

[79] Izvekov S and Voth G A 2006 Modeling real dynamics in the coarse-grained representation of condensed phase systems *J. Chem. Phys.* **125** 151101

[80] Vaz W L C and Almeida P F 1991 Microscopic versus macroscopic diffusion in one-component fluid phase lipid bilayer membranes *Biophys. J.* **60** 1553–4

[81] Falck E, Róg T, Karttunen M and Vattulainen I 2008 Lateral diffusion in lipid membranes through collective flows *J. Am. Chem. Soc.* **130** 44–5

[82] Carruthers A and Melchior D L 1983 Studies of the relationship between bilayer water permeability and bilayer physical state *Biochemistry* **22** 5797–807

[83] Jansen M and Blume A 1995 A comparative study of diffusive and osmotic water permeation across bilayers composed of phospholipids with different head groups and fatty acyl chains *Biophys. J.* **68** 997–1008

[84] Bloom M, Evans E and Mouritsen O G 1991 Physical properties of the fluid lipid-bilayer component of cell membranes: a perspective *Q. Rev. Biophys.* **24** 293–397

[85] Nagle J F, Mathai J C, Zeidel M L and Tristram-Nagle S 2008 Theory of passive permeability through lipid bilayers *J. Gen. Physiol.* **131** 77–85

[86] Paula S, Volkov A G, Vanhoek A N, Haines T H and Deamer D W 1996 Permeation of protons, potassium ions, and small polar molecules through phospholipid bilayers as a function of membrane thickness *Biophys. J.* **70** 339–48

[87] Orsi M, Sanderson W E and Essex J W 2009 Permeability of small molecules through a lipid bilayer: a multiscale simulation study *J. Phys. Chem.* B **113** 12019–29

[88] Rawicz W, Smith T J, McIntosh T, Simon S A and Evans E 2008 Elasticity, strength, and water permeability of bilayers that contain raft microdomain-forming lipids *Biophys. J.* **94** 4725–36

[89] Huster D, Jin A J, Arnold K and Gawrisch K 1997 Water permeability of polyunsaturated lipid membranes measured by ^{17}O NMR *Biophys. J.* **73** 855–64

[90] Mathai J C, Tristram-Nagle S, Nagle J F and Zeidel M L 2008 Structural determinants of water permeability through the lipid membrane *J. Gen. Physiol.* **131** 69–76

[91] Ollila S, Hyvönen M T and Vattulainen I 2007 Polyunsaturation in lipid membranes: dynamic properties and lateral pressure profiles *J. Phys. Chem.* B **111** 3139–50

[92] Melikov K C, Frolov V A, Shcherbakov A, Samsonov A V, Chizmadzhev Y A and Chernomordik L V 2001 Voltage-induced nonconductive pre-pores and metastable single pores in unmodified planar lipid bilayer *Biophys. J.* **80** 1829–36

[93] Riske K A and Dimova R 2005 Electro-deformation and poration of giant vesicles viewed with high temporal resolution *Biophys. J.* **88** 1143–55

[94] Michel J, Orsi M and Essex J W 2008 Prediction of partition coefficients by hybrid atomic level/coarse-grain simulations *J. Phys. Chem.* B **112** 657–60

[95] Cleaver D J, Care C M, Allen M P and Neal M P 1996 Extension and generalization of the Gay–Berne potential *Phys. Rev.* E **54** 559–67

[96] Price S L, Stone A J and Alderton M 1984 Explicit formulae for the electrostatic energy, forces and torques between a pair of molecules of arbitrary symmetry *Mol. Phys.* **52** 987–1001